Commun. Comput. Phys.
doi: 10.4208/cicp.160711.240212a

Vol. **13**, No. 2, pp. 540-558
February 2013

An Efficient Numerical Model for Immiscible Two-Phase Flow in Fractured Karst Reservoirs

Zhao-Qin Huang, Jun Yao* and Yue-Ying Wang

School of Petroleum Engineering, China University of Petroleum, Qingdao 266555, Shandong, China.

Received 16 July 2011; Accepted (in revised version) 24 February 2012

Communicated by Lianjie Huang

Available online 26 July 2012

Abstract. Numerical simulation of two-phase flow in fractured karst reservoirs is still a challenging issue. The triple-porosity model is the major approach up to now. However, the triple-continuum assumption in this model is unacceptable for many cases. In the present work, an efficient numerical model has been developed for immiscible two-phase flow in fractured karst reservoirs based on the idea of equivalent continuum representation. First, based on the discrete fracture-vug model and homogenization theory, the effective absolute permeability tensors for each grid blocks are calculated. And then an analytical procedure to obtain a pseudo relative permeability curves for a grid block containing fractures and cavities has been successfully implemented. Next, a full-tensor simulator has been designed based on a hybrid numerical method (combining mixed finite element method and finite volume method). A simple fracture system has been used to demonstrate the validity of our method. At last, we have used the fracture and cavity statistics data from TAHE outcrops in west China, effective permeability values and other parameters from our code, and an equivalent continuum simulator to calculate the water flooding profiles for more realistic systems.

AMS subject classifications: 35B27, 35Q30, 76S05

Key words: Fractured karst reservoirs, effective permeability tensor, discrete fracture-vug network model, two-phase flow, full-tensor simulator.

1 Introduction

Fractured karst reservoirs are composed of porous material, which contains cavities (or vugs) and fractures on multiple scales and throughout the entire rock formation [1]. The presence of fractures and cavities, often relatively large void spaces, affects the flow paths

*Corresponding author. *Email address:* rcogfr_upc@126.com (J. Yao)

in the medium and should be accurately accounted for in the numerical model. Modeling flow and transport processes in fractured karst reservoirs is still a challenging problem and the main difficulty is the co-existence of porous flow and free-fluid flow.

In the past 5 years, there are some scholars and engineers have paid much attention to the modeling single-phase flow in fractured karst carbonate reservoirs [2–9]. And their researches mainly focus on the equivalent absolute permeability analysis and the effect of the fractures and cavities based on homogenization of Stokes-Darcy equations or Stokes-Brinkman equations. Recently, in [10] and [11] Z.-Q. Huang and J. Yao et al. proposed a novel flow model named discrete fracture-vug network model (DFVN), which is efficient for single-phase flow in fractured karst carbonate reservoirs. The similar conceptual model also has been proposed by G. Qin et al. [12]. However, the multi-phase and two-phase flow based on discrete fracture-vug network model is still a challenging and open problem, since the governing equations of the free and porous flows are quite different from each other and involve both microscopic and macroscopic formulations.

As observed in carbonate formation, three porosity types (matrix, fractures, and cavities) are typically presented in naturally fractured karst reservoirs. These fractures and cavities distribute irregularly and vary in size, from microscopic to macroscopic. And the fractures and cavities are generally connected to form a fracture-cavity network [10, 11]. Drawing on the concept of dual-porosity model for fractured reservoirs, Y. S. Wu et al. proposed a triple-porosity model to study the flow and transport behaviors in fractured karst reservoirs [13–15]. And a field application was conducted in TAHE oilfield in west China [13]. However, the triple-continuum assumption is unacceptable for many cases.

In the presented paper, we will describe another alternative numerical model for immiscible two-phase flow in fractured karst reservoirs. There are three key steps in our approach. First, based on the discrete fracture-vug model and homogenization theory, the equivalent absolute permeability tensors (i.e., the ability to transmit fluids) for each grid block are calculated. Within this step only a steady-state single-phase flow model is used. In the next step, a pseudo relative permeability curves for each grid block containing fractures and cavities are obtained in an analytical procedure. The procedure is based on a fixed sequence of oil displacement from grid cells containing fractures and cavities: the volume of the fractures and cavities within a grid block is assumed to fill with water before the matrix volume of this grid-block is flooded (called the preferential flow assumption). This means that the fracture-vug network is the preferential flow path in grid blocks. In fractured karst reservoirs this is the main displacement sequence in waterflooding, at least for TAHE oilfield in west China. In the third step, a full-tensor reservoir simulator should be designed for this equivalent continuum model.

In the following Section we first outline the basis of our model and describe how we applied the discrete fracture-vug network to obtain the equivalent absolute permeability tensor. In Section 2.2 we describe the use of an analytical method to calculate the pseudo relative permeability curves in a grid block containing fracture-cavity network. In Section 3, a full tensor simulator has been designed based on a hybrid numerical method, in which the pressure equation is discretized using mixed finite element method and the

saturation is discretized by first-order finite volume method. In Section 4 some numerical cases are conducted for testing the validity of our approach. Finally, some conclusions are drawn in Section 5.

2 Equivalent continuum representation

The concept of equivalent continuum model was first proposed for single-phase flow in fractured reservoirs by Snow [16]. In the equivalent continuum model, the discontinuous nature of porosity and permeability in fractured reservoirs are represented by some averaged values of representative elementary volume (REV). The key step in modeling single-phase flow using this approach is to obtain the equivalent absolute permeability tensor. In the past half century, there are many people have made considerable efforts to calculate the equivalent absolute permeability by using analytical or numerical methods [17–21]. Recently, Arbogast et al. (see [3,4,8]), Popov et al. (see [1,5,6]) and Huang et al. (see [9,11]) applied the same principle to analyze the effective permeability of fractured karst reservoirs based on the homogenization theory. The simulation results for single-phase flow indicate that the equivalent continuum model is an efficient model for fractured karst reservoirs and is deserved to deep research for two-phase or multi-phase flow, especially for field-scale engineering problems. In the next sections, an efficient numerical model for immiscible two-phase flow in fractured karst reservoirs will be developed based on the equivalent continuum representation.

2.1 Effective permeability tensor for grid block

In our previous research [10], we have proposed the discrete fracture-vug network model (DFVN) to study the single-phase flow processes in fractured karst reservoirs. And a further research based on this novel model has been conducted to analyze the effective permeability tensor of the grid block [11]. Herein, we will just list some important parts and equations, please see [11] for detailed descriptions.

As shown in Fig. 1(a), the grid-block problem that are used to obtain effective permeability tensor of a grid block can be written as follows

$$-\nabla^2 \boldsymbol{w}_{\mathrm{s}}^j + \nabla \pi_{\mathrm{s}}^j = \boldsymbol{e}_j, \qquad \text{in } \Omega_{\mathrm{s}}, \tag{2.1a}$$

$$\nabla \cdot \boldsymbol{w}_{\mathrm{s}}^j = 0, \qquad \text{in } \Omega_{\mathrm{s}}, \tag{2.1b}$$

$$\boldsymbol{K}^{-1} \boldsymbol{w}_{\mathrm{d}}^j + \nabla \pi_{\mathrm{d}}^j = \boldsymbol{e}_j, \qquad \text{in } \Omega_{\mathrm{d}}, \tag{2.1c}$$

$$\nabla \cdot \boldsymbol{w}_{\mathrm{d}}^j = 0, \qquad \text{in } \Omega_{\mathrm{d}}, \tag{2.1d}$$

$$\boldsymbol{w}_{\mathrm{s}}^j \cdot \boldsymbol{n}_{\mathrm{s}} = \boldsymbol{w}_{\mathrm{d}}^j \cdot \boldsymbol{n}_{\mathrm{s}}, \qquad \text{on } \Sigma, \tag{2.1e}$$

$$2\boldsymbol{n}_{\mathrm{s}} \cdot \boldsymbol{D}(\boldsymbol{w}_{\mathrm{s}}^j) \cdot \boldsymbol{n}_{\mathrm{s}} = \pi_{\mathrm{s}}^j - \pi_{\mathrm{d}}^j, \qquad \text{on } \Sigma, \tag{2.1f}$$

$$\boldsymbol{w}_{\mathrm{s}}^j \cdot \boldsymbol{\tau}_{\mathrm{s}} = -2\frac{\sqrt{\boldsymbol{\tau}_{\mathrm{s}} \cdot \boldsymbol{K} \cdot \boldsymbol{\tau}_{\mathrm{s}}}}{\alpha} \boldsymbol{n}_{\mathrm{s}} \cdot \boldsymbol{D}(\boldsymbol{w}_{\mathrm{s}}^j) \cdot \boldsymbol{\tau}_{\mathrm{s}}, \qquad \text{on } \Sigma, \tag{2.1g}$$

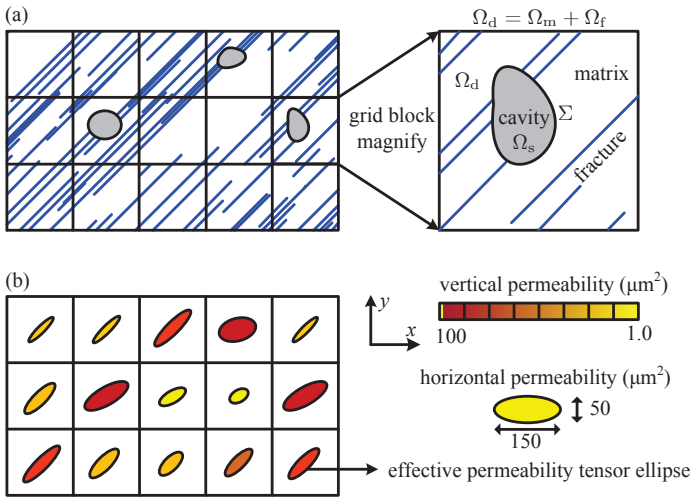

Figure 1: A simple fracture-cavity system (top) and its corresponding map of grid block effective permeability tensor ellipses (bottom).

where $\boldsymbol{w}_l^j$ and π_l^j ($l=s,d$, here s denotes Stokes flow domain and d denotes Darcy porous flow domain) are the periodic vector fields. $\boldsymbol{e}_j$ is the unit vector along j-th direction, $\boldsymbol{n}_s$ is the normal vector of the interface between Ω_s and Ω_d, $\boldsymbol{D}(\boldsymbol{w}_s^j)=(\nabla \boldsymbol{w}_s^j+\boldsymbol{w}_s^j\nabla)/2$ is the strain rate, $\boldsymbol{\tau}_s$ is the unit tangential vector of interface Σ (as illustrated in Fig. 1(a)), α is the Beavers-Joseph-Saffman slip coefficient [22, 23]. The effective permeability tensor $\boldsymbol{\kappa}$ of a grid block is then computed by averaging the fine-scale velocities

$$\boldsymbol{\kappa}=\frac{1}{|\Omega|}\Big(\int_{\Omega_s}\boldsymbol{w}_s^j d\Omega+\int_{\Omega_d}\boldsymbol{w}_d^j d\Omega\Big) \tag{2.2}$$

and its components are given as

$$\kappa_{ij}=\frac{1}{|\Omega|}\Big[\int_{\Omega_s}(\boldsymbol{w}_s^j)_i d\Omega+\int_{\Omega_d}(\boldsymbol{w}_d^j)_i d\Omega\Big],$$

where

$$\int_{\Omega_d}(\boldsymbol{w}_d^j)_i d\Omega=\int_{\Omega_m}(\boldsymbol{w}_m^j)_i d\Omega+e\times\int_{\Omega_f}(\boldsymbol{w}_f^j)_i d\Omega.$$

Here, e is the aperture of fracture. It can be proved that $\boldsymbol{\kappa}$ is symmetric and positive definite [11].

Through the above up-scaling procedure, the effective permeability tensor of every grid blocks can be obtained and the map of corresponding tensor ellipses will be descried as shown in Fig. 1(b). Noting that if there is not any cavities or vugs, the cell problem could be simplified to a discrete fractures system.

2.2 Pseudo relative permeability curves

The key issue to tracking the rapid water advance due to the presence of conductive fractures and cavities is to obtain the effective relative permeability. Herein, we use the pseudo relative permeability curves in our numerical model. However, the use of pseudo relative permeability curves is not a new concept. Hearn (1971) [24] firstly introduced the concept of pseudo relative permeability curves for modeling stratified water flooding. Telleria et al. (1999) [25] also used the same functions to study stratified systems under no cross flow and found some restricts in their application. van Golf-Rach (1982) [18] pointed to the possibility of using laboratory core results to build pseudo relative permeability curves for fracture reservoirs. Pruess et al. (1990) [26] derived some simple formulas for effective continuum characteristic curves in terms of the properties of fracture and matrix continua, respectively. Van Lingen et al. (2001) [27] presented a technique which modifies the relative permeability curves analytically to produce pseudo relative permeability curves for the grid blocks containing fractures. Their method does not require grid modification (refinement) for these grid blocks. Recently, Rida Abdel-Ghani (2009) [28] describes a modified pseudo relative permeability correlation, which is based on the van Lingen et al. method that exaggerates the water breakthrough time and water cut predictions, especially in the low to medium fracture-to-matrix permeability contrast cases.

In the present work, we will extend Rida Abdel-Ghani's method to the fractured karst reservoirs. And the curves are calculated analytically, based on the preferential flow assumption that the fracture-cavity network volume of a grid block is filled with water prior to imbibition of water into the matrix. For a grid block containing fractures and cavities, the total porosity of a grid block can be calculate as the following arithmetic average

$$\phi_{\mathrm{b}}=\phi_{\mathrm{m}}+\phi_{\mathrm{f}}+\phi_{\mathrm{c}}=\phi_{\mathrm{m}}+\frac{\sum e_i l_i}{V}+\frac{\sum (V_{\mathrm{c}})_j}{V}, \tag{2.3}$$

where ϕ_{m}, ϕ_{f} and ϕ_{c} are the matrix porosity, fracture porosity and cavity porosity respectively, e_i and l_i are the i-th fracture's aperture and length, $(V_{\mathrm{c}})_j$ is the j-th cavity's volume, V is the volume of the given grid block. Note that both the inner porosity in fractures and cavities are taken as 1.

Pseudo End-Points: The effective residual saturations and end-point relative permeabilities of grid blocks are changed by the presence of discrete fracture-cavity networks. The effective residual oil saturation of a fractured karst gird block $S_{\mathrm{or,b}}$ is calculated using the following arithmetic average

$$S_{\mathrm{or,b}}=\frac{\phi_{\mathrm{m}}S_{\mathrm{or,m}}+(\phi_{\mathrm{f}}+\phi_{\mathrm{c}})S_{\mathrm{or,fc}}}{\phi_{\mathrm{m}}+\phi_{\mathrm{f}}+\phi_{\mathrm{c}}}, \tag{2.4}$$

where $S_{\mathrm{or,m}}$ is the residual oil saturation in the matrix and $S_{\mathrm{or,fc}}$ is the residual oil saturation in the discrete fracture-cavity network. Similarly, the effective connate water

saturation of a gird block $S_{wc,b}$ is calculated as

$$S_{wc,b}=\frac{\phi_m S_{wc,m}+(\phi_f+\phi_c)S_{wc,fc}}{\phi_m+\phi_f+\phi_c}, \tag{2.5}$$

where $S_{wc,m}$ is the connate water saturation in the matrix, and $S_{wc,fc}$ is the connate water saturation in the discrete fracture-cavity network.

End-Point Relative Permeabilities: The effective end-point relative permeability $k_{oe,b}$ to oil in grid blocks containing fracture-cavity networks is obtained by

$$k_{oe,b}=\frac{k_{oe,m}k_m\phi_m+k_{oe,fc}k_{fc}(\phi_f+\phi_c)}{k_m\phi_m+k_{fc}(\phi_f+\phi_c)}, \tag{2.6}$$

where $k_{oe,m}$ is the matrix end-point relative permeability at the residual water saturation and $k_{oe,fc}$ is the end-point relative permeability in fracture-cavity network system. $k_m=\text{trace}(\boldsymbol{K}_m)/n$, in which n is the dimensions in space and $\boldsymbol{K}_m$ is the matrix permeability tensor. $k_{fc}=\text{trace}(\boldsymbol{K}_{fc})/n$ and $\boldsymbol{K}_{fc}$ is defined by the following formulation

$$\boldsymbol{\kappa}=\boldsymbol{K}_m+\boldsymbol{K}_{fc}. \tag{2.7}$$

It is clear that all the three tensors in Eq. (2.7) are symmetric and positive definite. Here we assumed that the relative permeabilities are direction invariant, which is a common assumption for modeling multi-phase flow in porous media. Similarly, the effective end-point relative permeability $k_{we,b}$ to water in grid block can be calculated as

$$k_{we,b}=\frac{k_{we,m}k_m\phi_m+k_{we,fc}k_{fc}(\phi_f+\phi_c)}{k_m\phi_m+k_{fc}(\phi_f+\phi_c)}, \tag{2.8}$$

where, $k_{we,m}$ is the end-point relative permeability at the connate water saturation in the matrix and $k_{we,fc}$ is the end-point relative permeability at the connate water saturation in the fracture-cavity network.

Relative Permeability Curves: As mentioned earlier, matrix and fracture-cavity system relative permeability curves are combined under the preferential flow assumption. The procedure of generating pseudo relative permeability curves is illustrated in Fig. 2. First, we should normalize the original matrix and fracture-cavity curves between 0 and 1, respectively.

The parameters in Fig. 2(c) required to combine the matrix and the fracture-cavity relative permeabilities are defined as following

$$\alpha_{fc}=\frac{(1-S_{wc,fc}-S_{or,fc})(\phi_f+\phi_c)}{(1-S_{wc,fc}-S_{or,fc})(\phi_f+\phi_c)+(1-S_{wc,m}-S_{or,m})\phi_m} \tag{2.9}$$

represents the contribution of the fracture-cavity volume to the total mobile porosity in a grid block. $\beta_{fc,w}$ is the contribution of fracture-cavity system to the maximum grid block

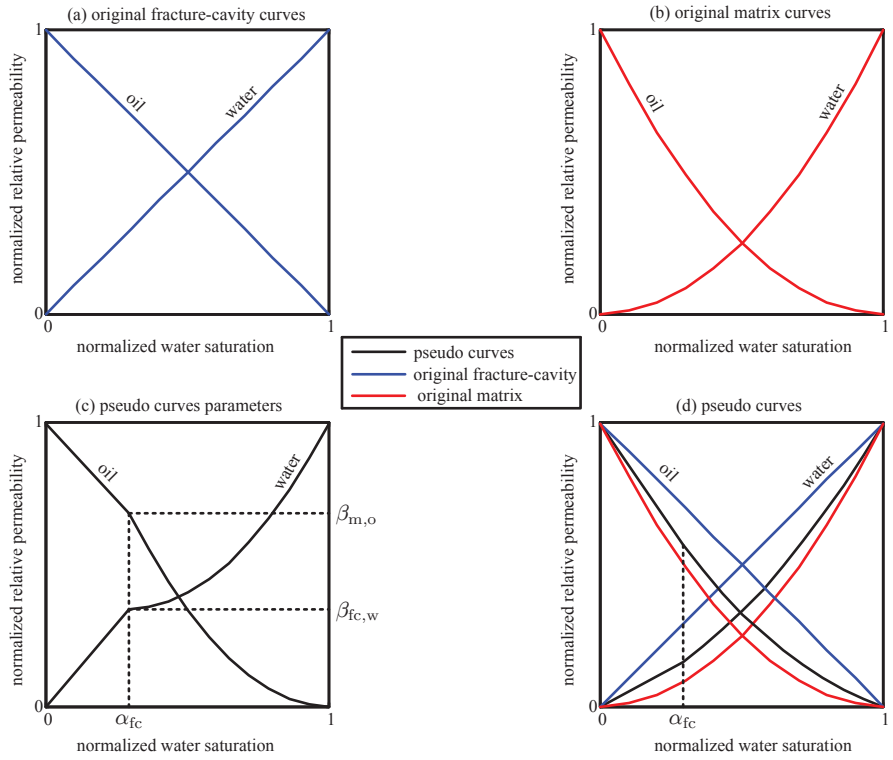

Figure 2: Generation of pseudo permeability curves by combining the original fracture-cavity and the matrix relative permeability curves.

relative permeability to water, which defined as

$$\beta_{fc,w} = \frac{k_{fc}k_{we,fc}(\phi_f+\phi_c)}{k_{fc}k_{we,fc}(\phi_f+\phi_c)+k_m k_{we,m}\phi_m}. \tag{2.10}$$

$\beta_{m,o}$, the contribution of matrix to the maximum grid block relative permeability to oil, is defined as

$$\beta_{m,o} = \frac{k_m k_{oe,m}\phi_m}{k_{fc}k_{oe,fc}(\phi_f+\phi_c)+k_m k_{oe,m}\phi_m}. \tag{2.11}$$

And then the new normalized points from the original matrix curves are calculated as the following transformations

$$\begin{cases} S^*_{wn,b} = S_{wn,m}(1-\alpha_{fc})+\alpha_{fc}, \\ k^*_{rw,b} = k_{rw,m}+(S^*_{wn,b}-k_{rw,m})\beta_{fc,w}, \\ k^*_{ro,b} = k_{ro,m}+(1-S^*_{wn,b}-k_{ro,m})(1-\beta_{m,o}). \end{cases} \tag{2.12}$$

Here we assume that the normalized relative permeability curves of fracture-cavity systems are the widely known straight line curves (cf. Fig. 2(a)). Note that the pseudo

permeability curves should be limited in the original matrix and fracture-cavity curves (cf. Fig. 2(d)).

Then, the quantitative evaluation of the effective continuum capillary pressure is straightforward. Based the preferential flow assumption, there are two flow stage in a grid block containing fracture-cavity networks, i.e., the preferential flow stage in the fracture-cavity network and the second stage flow in matrix. So given a certain average water saturation of grid block $S_{\mathrm{w,b}}$, the corresponding water saturation $S_{\mathrm{w,m}}$ and $S_{\mathrm{w,fc}}$, in fracture-cavity system and matrix can be found from the following equation

$$S_{\mathrm{w,b}}=\frac{\phi_{\mathrm{m}}S_{\mathrm{w,m}}+(\phi_{\mathrm{f}}+\phi_{\mathrm{c}})S_{\mathrm{w,fc}}}{\phi_{\mathrm{m}}+\phi_{\mathrm{f}}+\phi_{\mathrm{c}}}. \tag{2.13}$$

The capillary pressure could be found from the capillary functions of the fracture-cavity system and matrix, respectively.

3 Full-tensor numerical simulator

Usually the effective permeability of a grid block is a full tensor. A diagonal tensor only occurs if the computational grid is aligned with the principal axes of the general tensor. So an efficient full-tensor reservoir simulator should be designed for the pressure equation. There are some full-tensor schemes have been developed in recent years (such as [29–32]) that impose the continuous flux and pressure constraints via locally coupled algebraic systems. In this paper, we will use mixed finite element method (Mixed FEM) to solve the non-homogeneous and anisotropic pressure equation. Simultaneously, the finite volume method (FVM) is applied to solve the saturation equation.

3.1 The two-phase model

We consider immiscible and incompressible flow of two phases (oil and water) and assume no-flow boundary conditions. The flow equations can then be formulated as an elliptic equation for the globe pressure p and the total Darcy velocity $\boldsymbol{v}$ (the details can be found in [37]),

$$\boldsymbol{v}=-\boldsymbol{\kappa}\lambda\cdot\nabla p+\boldsymbol{\kappa}\lambda\cdot(\lambda_{\mathrm{w}}\rho_{\mathrm{w}}+\lambda_{\mathrm{o}}\rho_{\mathrm{o}})\boldsymbol{G},\qquad \nabla\cdot\boldsymbol{v}=q, \tag{3.1}$$

where q is a source term representing injection and production wells, $\boldsymbol{\kappa}$ is the grid blocks' effective permeability tensor and $\lambda=\lambda_{\mathrm{o}}+\lambda_{\mathrm{w}}$ denotes the total mobility. The mobility of phase is given by $\lambda_l=k_{\mathrm{r}l}/\mu_l$, where μ_l is viscosity of phase l and $k_{\mathrm{r}l}(S_{\mathrm{w}})$ is the relative permeability. $\boldsymbol{G}=-g\nabla z$ is the gravitational pull-down force, where g is the gravitational constant and z is the spatial coordinate in the upward vertical direction. The second primary unknown is the water saturation S_{w}, which denotes the volume fraction of water

and is described by the transport equation

$$\phi\frac{\partial S_{\rm w}}{\partial t}+\nabla\cdot\boldsymbol{v}_{\rm w}=q_{\rm w}, \tag{3.2a}$$

$$\boldsymbol{v}_{\rm w}=f_{\rm w}\left[\boldsymbol{v}+\boldsymbol{\kappa}\lambda_o\cdot\nabla p_{\rm cow}+\boldsymbol{\kappa}\lambda_{\rm o}\cdot(\rho_{\rm w}-\rho_{\rm o})\boldsymbol{G}\right], \tag{3.2b}$$

where ϕ is the grid block' porosity, $f_{\rm w}=\lambda_{\rm w}/\lambda$ is the fractional flow function and $p_{\rm cow}$ is the capillary pressure.

The system of Eqs. (3.1)-(3.2b) will be solved using an IMPES sequential splitting scheme, i.e., the pressure equation is solved at the current time-step using saturation values from the previous time-step, then the total velocity $\boldsymbol{v}$ is kept constant as a parameter in Eq. (3.2a), while the saturation is advanced in time.

3.2 Mixed FEM for pressure equation

In this section, we describe a mixed finite element method for the accurate approximation of the globe pressure equation (3.1). This method conserves mass cell by cell and produces a direct approximation of the two variables pressure and velocity. The mixed finite element formulation of Eq. (3.1) reads: find $(p,\boldsymbol{v})\in L^2(\Omega)\times H_0^{1,\rm div}(\Omega)$, such that

$$\begin{aligned}\int_\Omega \boldsymbol{u}\cdot\left[\boldsymbol{\kappa}\lambda(S_{\rm w}^k)\right]^{-1}\cdot\boldsymbol{v}^{k+1}\,{\rm d}\Omega-\int_\Omega p^{k+1}\nabla\cdot\boldsymbol{u}\,{\rm d}\Omega\\ =\int_\Omega \boldsymbol{u}\cdot\left[f_{\rm w}(S_{\rm w}^k)\rho_{\rm w}+f_{\rm o}(S_{\rm w}^k)\rho_{\rm o}\right]\boldsymbol{G}\,{\rm d}\Omega,\end{aligned} \tag{3.3a}$$

$$\int_\Omega l\nabla\cdot\boldsymbol{v}^{k+1}\,{\rm d}\Omega=\int_\Omega lq^{k+1}\,{\rm d}\Omega \tag{3.3b}$$

for all $\boldsymbol{u}\in H_0^{1,\rm div}(\Omega)$ and $l\in L^2(\Omega)$. Here the superscript k denotes the k-th time step. Next we introduce the lowest order Raviart-Thomas RT_0 space [33] as follows

$$P=\left\{p\in L^2(\Omega):p\big|_{\Omega_i}\text{ is constant }\forall\Omega_i\in\Omega\right\}, \tag{3.4a}$$

$$\begin{aligned}V=\Big\{&\boldsymbol{v}\in H_0^{1,\rm div}(\Omega):\boldsymbol{v}\big|_{\Omega_i}\text{ have linear components }\forall\Omega_i\in\Omega,\\ &(\boldsymbol{v}\cdot\boldsymbol{n}_{ij})\big|_{\gamma_{ij}}\text{ is constant }\forall\gamma_{ij}\in\Omega,\text{ and }\boldsymbol{v}\cdot\boldsymbol{n}_{ij}\text{ is continuous across }\gamma_{ij}\Big\}.\end{aligned} \tag{3.4b}$$

Here, γ_{ij} is the interface between cell Ω_i and cell Ω_j, $\boldsymbol{n}_{ij}$ is the unit normal to γ_{ij} pointing from Ω_i to Ω_j. The corresponding Raviart-Thomas mixed FEM thus seeks

$$(p,\boldsymbol{v})\in P\times V,\text{ such that (3.3) holds for all }\boldsymbol{u}\in V\text{ and }l\in P. \tag{3.5}$$

To express equation system (3.3) as a linear system, observe that functions in V are, for admissible grids, spanned by base functions $\{\boldsymbol{w}_{ij}\}$ that are defined by

$$\{\boldsymbol{w}_{ij}\}\in\mathcal{P}(\Omega_i)^d\cup\mathcal{P}(\Omega_j)^d\quad\text{and}\quad\int_{\gamma_{kl}}\boldsymbol{w}_{ij}\cdot\boldsymbol{n}_{kl}\,{\rm d}\Gamma=\begin{cases}1, & \text{if }\gamma_{kl}=\gamma_{ij},\\ 0, & \text{else,}\end{cases}$$

where $\mathcal{P}(\mathcal{M})$ is a set of linear functions on $\mathcal{M}$. Similarly,

$$U=\text{span}\{\psi_m\} \quad \text{and} \quad \chi_m=\begin{cases} 1, & \text{if } \boldsymbol{x}\in\Omega_m, \\ 0, & \text{else.} \end{cases}$$

Thus, we can write the approximations $\hat{p}=\sum_{\Omega_m} p_m\psi_m$ and $\hat{\boldsymbol{v}}=\sum_{\gamma_{ij}} v_{ij}\boldsymbol{w}_{ij}=\boldsymbol{W}\boldsymbol{v}$.

Then, Eq. (3.3) can be written as the following element assembly forms

$$\sum_{\Omega_e}\Big(\int_{\Omega_e}\boldsymbol{W}_e^{\mathrm{T}}\cdot\lambda_e^{-1}\cdot\boldsymbol{W}_e\,\mathrm{d}\Omega\boldsymbol{v}_e\Big)-\sum_{\Omega_e}\Big(\int_{\Omega_e}\nabla\cdot\boldsymbol{W}_e^{\mathrm{T}}\,\mathrm{d}\Omega\,p_e\Big)=\sum_{\Omega_e}\Big(\int_{\Omega_e}\boldsymbol{W}_e^{\mathrm{T}}\cdot\rho\boldsymbol{G}_e\,\mathrm{d}\Omega\Big), \tag{3.6a}$$

$$\sum_{\Omega_e}\Big(\int_{\Omega_e}\nabla\cdot\boldsymbol{W}_e\,\mathrm{d}\Omega\,\boldsymbol{v}_e\Big)=\sum_{\Omega_e}\Big(\int_{\Omega_e}q\,\mathrm{d}\Omega\Big), \tag{3.6b}$$

and this system takes the form

$$\begin{bmatrix}\boldsymbol{B} & -\boldsymbol{C}^{\mathrm{T}}\\ \boldsymbol{C} & 0\end{bmatrix}\begin{bmatrix}\boldsymbol{v}\\ \boldsymbol{p}\end{bmatrix}=\begin{bmatrix}\boldsymbol{g}\\ \boldsymbol{q}\end{bmatrix}. \tag{3.7}$$

The interested reader is referred to [33–37] for more details.

3.3 FVM for saturation equation

In this section, we describe the finite volume method used for the approximation of the saturation equation. Only a short description of the method employed in this paper will be given. The interested reader is referred to [37–40] for more details. The saturation discretization in the i-th grid block based on finite volume method is given as

$$\int_{\Omega_i}\phi\frac{\partial S}{\partial t}\,\mathrm{d}\Omega+\int_{\partial\Omega_i}\big(f_{\mathrm{w}}(\boldsymbol{v}+\boldsymbol{\kappa}\lambda_{\mathrm{o}}\cdot\nabla p_{\mathrm{cow}}+\boldsymbol{\kappa}\lambda_{\mathrm{o}}\cdot(\rho_{\mathrm{w}}-\rho_{\mathrm{o}})\boldsymbol{G})\big)\cdot\boldsymbol{n}_i\,\mathrm{d}\Gamma=\int_{\Omega_i}q_{\mathrm{w}}\,\mathrm{d}\Omega. \tag{3.8}$$

Here we dropped the subscript w for water saturation S_{w}. Using the θ-rule for temporal discretization, a finite-volume scheme takes the following form

$$\frac{\phi_i}{\Delta t}(S_i^{k+1}-S_i^k)+\frac{1}{|\Omega_i|}\sum_{\gamma_{ij}}\big(\theta F_{ij}(S^{k+1})+(1-\theta)F_{ij}(S^k)\big)=q_{\mathrm{w}}(S_i^k), \tag{3.9}$$

where

$$F_{ij}(S)=\int_{\gamma_{ij}}f_{\mathrm{w}}(S)_{ij}(\boldsymbol{v}\cdot\boldsymbol{n}_{ij}+\boldsymbol{\kappa}\lambda_{\mathrm{o}}\cdot\nabla p_{\mathrm{cow}}\cdot\boldsymbol{n}_{ij}+\boldsymbol{\kappa}\lambda_{\mathrm{o}}\cdot(\rho_{\mathrm{w}}-\rho_{\mathrm{o}})\boldsymbol{G}\cdot\boldsymbol{n}_{ij})\,\mathrm{d}\Gamma$$

is a numerical approximation of the flux over edge γ_{ij}. For a first-order scheme, it is common to use upstream weighting for the fractional flow

$$f_{\mathrm{w}}(S)_{ij}=\begin{cases} f_{\mathrm{w}}(S_i), & \text{if } \boldsymbol{v}\cdot\boldsymbol{n}_{ij}\geqslant 0, \\ f_{\mathrm{w}}(S_j), & \text{if } \boldsymbol{v}\cdot\boldsymbol{n}_{ij}<0. \end{cases} \tag{3.10}$$

In this paper an explicit scheme, i.e., θ=0, is employed. Such scheme is quite accurate but need impose stability restrictions on the time step, i.e., the CFL condition,

$$\Delta t \leqslant \frac{\phi_i|\Omega_i|}{v_i^{\text{in}}\max\{f_{\text{w}}'(S)\}_{0\leqslant S\leqslant 1}},$$

where

$$v_i^{\text{in}} = \max(q_i,0) - \sum_{\gamma_{ij}} \min(v_{ij},0), \qquad \frac{\partial f_{\text{w}}}{\partial S} = \frac{\partial f_{\text{w}}}{\partial S^*}\frac{\partial S^*}{\partial S} = \frac{1}{1-S_{\text{wc}}-S_{\text{or}}}\frac{\partial f_{\text{w}}}{\partial S^*},$$

here S^* denotes the normalized water saturation.

4 Numerical results

4.1 Numerical validation

Before proceeding to the examples for fractured karst reservoirs, we first test the numerical validation from a model in a simple fractured medium (a fracture can be consider a special cavity). We consider a single fracture in the matrix block. Waterflooding simulations are carried out for two different orientations of the fracture $(\theta = 0, \pi/4)$. Fig. 3(a) is the geometrical configuration. We consider a fracture thickness e=100 μm $(k_{\text{f}} = 8.37\times 10^5 \mu\text{m}^2)$. The porosity and the permeability of the matrix are ϕ=1.0 and $k_{\text{m}} = 1\mu\text{m}^2$, respectively. The medium is initially filled with oil. We inject water at the bottom left corner at the rate of q=0.01PV/day. Liquid is produced from the top right corner at the same rate of injector.

For simplicity, we neglect the gravity and capillary effects and the original matrix and fracture permeability curves are straight lines as shown in Fig. 2(a). As discussed in Section 3.2, the pseudo relative permeability curves is also the straight lines. The connate water saturation and residual oil saturation are both zero.

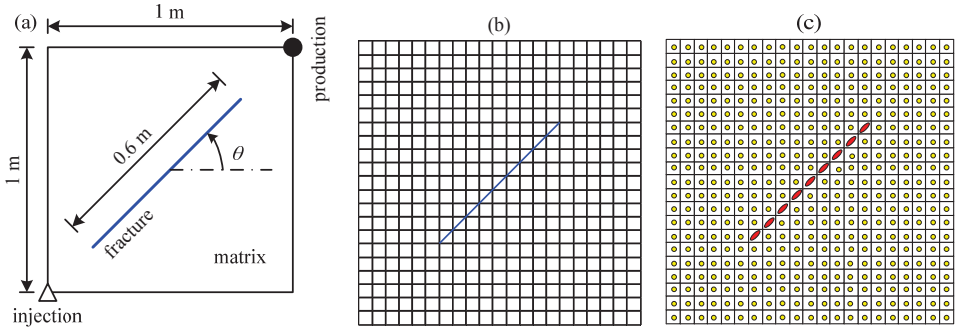

Figure 3: Geometrical configuration of the fractured media with a single fracture (left) and a mesh of grid blocks (medium) and its corresponding permeability tensor map (right).

First, We generated a mesh of grid blocks for the region, by uniformly subdividing it into 21×21 grid blocks, as illustrated in Fig. 3(b). Here we just show the inclined fracture case with $\theta=\pi/4$. Fig. 3(c) illustrates the corresponding effective permeability tensor ellipses.

Then let us evaluate the validation and accuracy of the present equivalent continuum model by comparing the results with those obtained by the discrete-fracture model [41]. Two different meshes of grid blocks are considered, one is 21×21 and the other is 31×31. Fig. 4 presents the water saturation profile at 0.5PV water injection. As can be seen, the results from the equivalent continuum model are in excellent agreement with the discrete-fracture model. It also implies that the numerical results will be more satisfied with the refining of the mesh.

4.2 Complex fractured karst reservoir 1

In this section, we applied our approach to a fractured karst system generated with statistical data from a naturally fractured karst carbonate reservoir outcrop. The reservoir we chose was in the TAHE oilfield in west China. Some of the fracture statistics for fractures system are presented in Table 1. And the cavities are simplified into some ellipses with some statistics characteristics, which are presented in Table 2. Using these data, we generated the realization of the fractured karst system depicted in Fig. 5(a). The size of this region is 100m$\times$200m $(x\times y)$.

Table 1: Macro fractures' statistic data.

Property	Minimum value	Maximum value	Average value
Length, m	20	160	65.2
Orientation, degrees	45	45	45
Intensity, $1/m$	0.14	0.58	0.33

Table 2: Macro cavities' statistic data.

Property	Minimum value	Maximum value	Average value
Axis length, m	2.1	8.3	6.5
Orientation, degrees	0	15	5.0
Density, $1/km^2$	1026	2100	1750

Then we generated a mesh of grid blocks for the region, by uniformly subdividing it into 10×20 grid blocks, as illustrated in Fig. 5(b). The permeability map along y-direction is presented in Fig. 5(c). From this map we can see that the fracture-cavity networks have an important influence in the effective permeability and they are the main factors for heterogeneity of formation.

We chose a matrix permeability of $k_{\rm m}=1\mu m^2$ and a uniform fracture aperture of 100μm ($k_{\rm f}=8.37\times10^5\mu m^2$). The porosity and effective permeability tensor are calculated

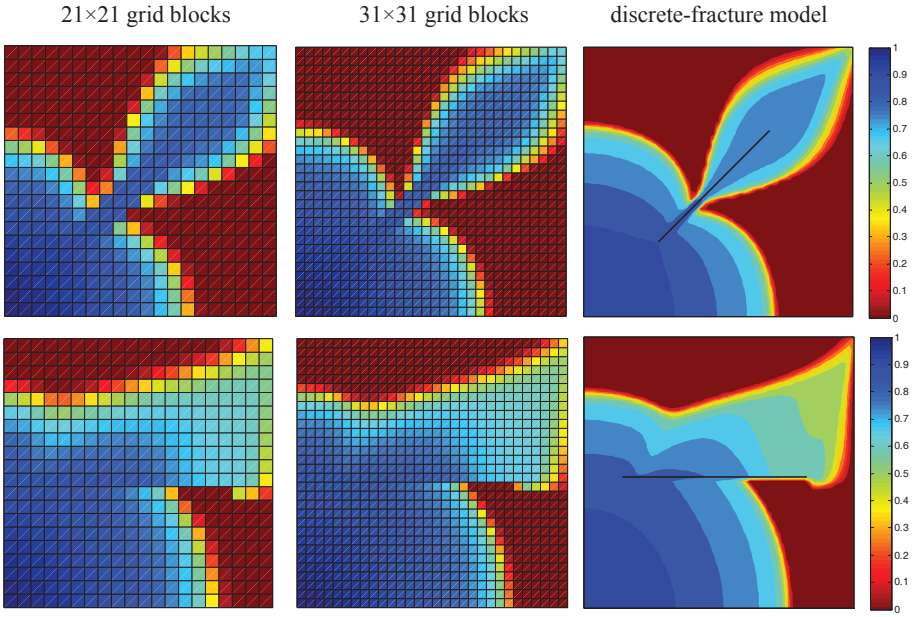

Figure 4: Water saturation profiles at 0.5PV water injection: simple fractured media with a single fracture, one with a titled fracture (top) and one with horizontal fracture (bottom).

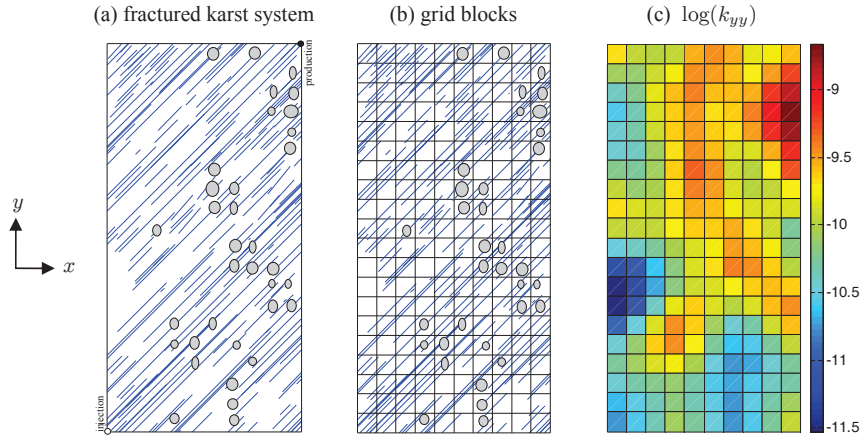

Figure 5: Realization of a fractured karst system generated with the statistics corresponding to the TAHE outcrop from Tables 1 and 2 (left); the mesh of grid blocks (medium); the permeability logarithm map along y-direction (right).

by using Eqs. (2.2) and (2.3). For simplicity, we also neglect the gravity and capillary effects and the original normalized fracture-cavity relative permeability curves are straight lines and the origin normalized matrix relative permeability curves are $k_{\mathrm{rw,m}}=(S^*_{\mathrm{w,m}})^2$ and $k_{\mathrm{ro,m}}=(1-S^*_{\mathrm{w,m}})^2$. Both the connate water saturation and residual saturation of matrix and fracture-cavity system are zero. The pseudo relative permeability curves for

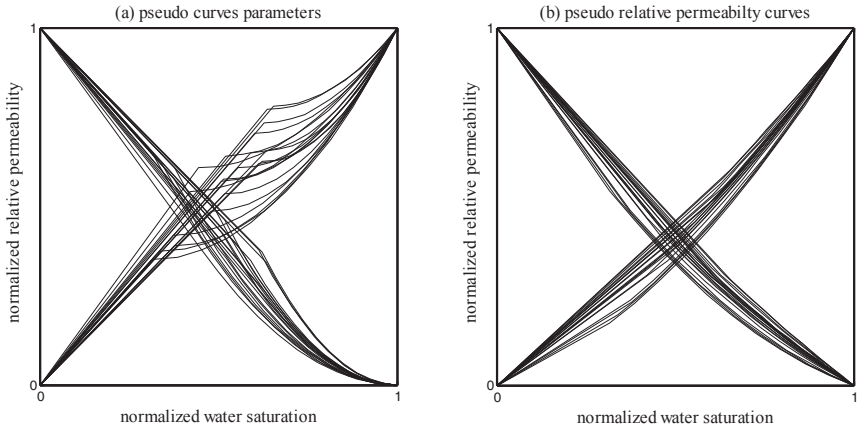

Figure 6: Pseudo curve parameters (as shown in Fig. 3(c)) determination for each grid blocks (left) and the corresponding pseudo relative permeability curves of grid blocks (right).

some grid blocks are shown in Fig. 6(b). The medium is initially filled with oil. We inject water at the bottom left corner at the rate of $q=0.004$PV/day. Liquid is produced from the top right corner at the same rate of injector.

Fig. 7 shows the influence of variations in the effective parameters on the motion of the water through the fractured karst region. Three snapshots of the subsequent evolution of the water flooding are presented in the figure. They help to illustrate how fluid moves through the homogenized grid blocks. In the figure, we can see that the variations in the effective permeability and pseudo relative permeability curves have had a pronounced and cumulative effect on the flow through the region.

In Fig. 7, we also superimpose the fracture-cavity system onto a plot of the water saturation profile at 0.5PV water injection. We can see that the fluid flow is primarily determined by the orientation and intensity of fracture-cavity system. The figure shows that the preferred direction of motion is primarily determined by the properties of the fracture-cavity system. And the corresponding effective parameters of the homogenized grid blocks honors these properties.

4.3 Complex fractured karst reservoir 2

In the above example, the fractures are aligned with the same direction. In this section, we will give a more general case with fractures in multiple directions. As illustrated in Fig. 8(a), the size of the study domain is 100 m$\times$100m $(x\times y)$, where the coordinate system is as same as that of the complex fractured karst reservoir 1 depicted in Fig. 5. One would note that the fracture network is an orthogonal fracture system. The permeability of matrix $k_{\rm m}=11\mu$m^2 and a uniform fracture aperture of 100μm $(k_{\rm f}=8.37\times10^5\mu$m$^2)$. The medium is initially filled with oil. We inject water at the bottom left corner at the rate of $q=0.01$PV/day. Liquid is produced from the top right corner at the same rate of injector.

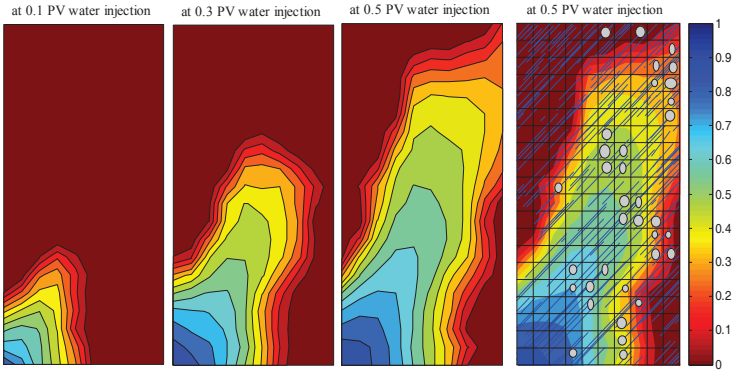

Figure 7: Three water saturation profiles at different times and the superposition of the fracture-cavity system on the evolved water saturation map.

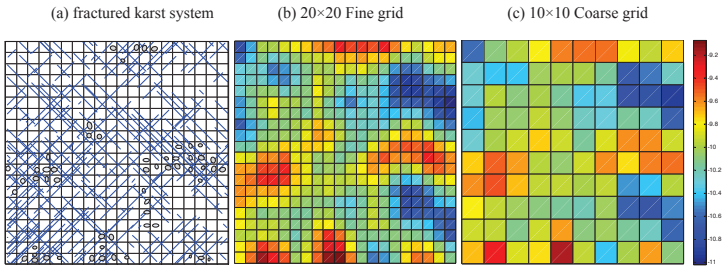

Figure 8: A conceptual fractured karst system (left); the permeability logarithm map along x-direction at the fine grid (medium); the corresponding permeability logarithm map along x-direction at the coarse grid (right).

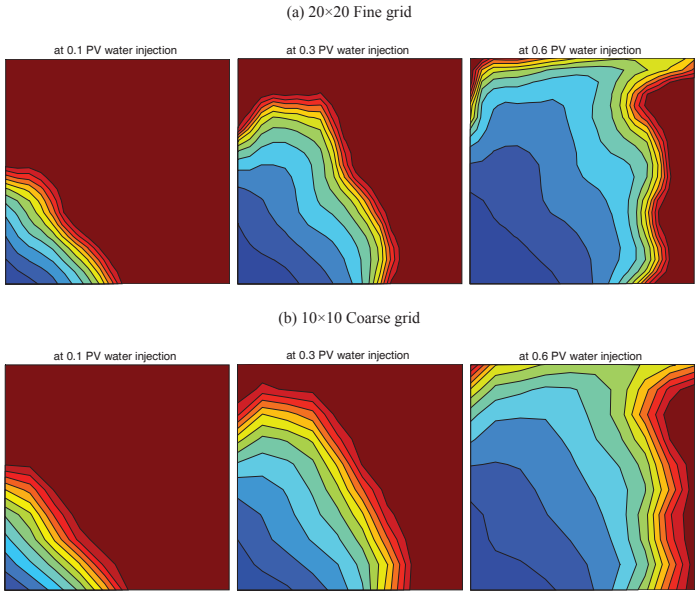

Figure 9: Comparison with water saturation profiles between the fine grid (top) and the coarse grid (bottom) at different times.

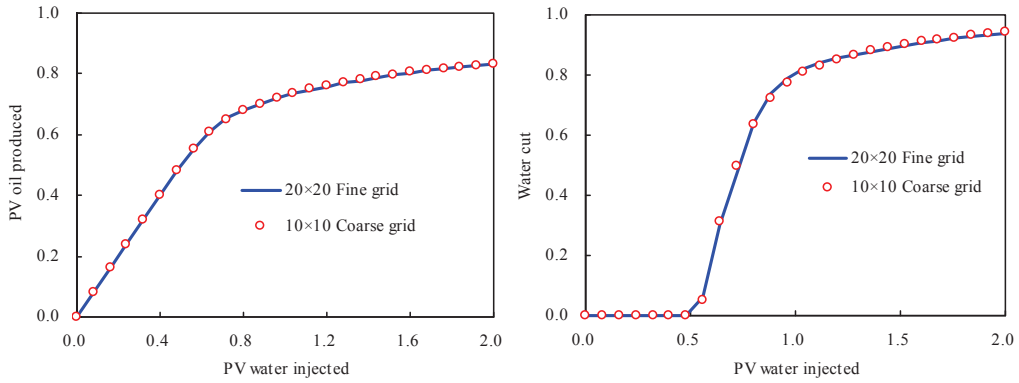

Figure 10: Comparison with cumulative oil production between the fine grid and the coarse grid (left); and water cut curves for the fine grid and the coarse grid (right).

The other parameters are the same as those given in Section 4.2. Following the same procedure, the pseudo relative permeability curves for each grid block can be evaluated. For concise, the corresponding figures are not listed here, which are similar to Fig. 6. In order to verify the validity of our approach, two mesh gridding scheme are conducted as depicted in Fig. 8.

The influence of variations in the effective parameters on the motion of the water through the fractured karst region are shown in Fig. 9. Three snapshots of the subsequent evolution of the water flooding with different grid systems are presented in this figure. They help to illustrate how fluid moves through the homogenized grid blocks. From Fig. 9, we can see that the variations in the effective permeability and pseudo relative permeability curves have had a pronounced and cumulative effect on the flow through the region. Simultaneously, the evolution of the water saturation at the coarse grid are more smooth since the heterogeneity of the reservoir is homogenized at coarse grid. Fig. 10 presents the cumulative oil production and water cut for both two grid systems until 2PV water injection. We observe very close agreement between the two grid systems, which again demonstrate the validity of our approach.

5 Conclusions

The main conclusions of this study can be summarized as follows: 1. We have successfully implemented an efficient numerical code to calculate the effective permeability tensor of grid blocks based on Darcy-Stokes coupling equations and homogenization theory. On the basis of the preferential flow assumption, an analytical calculation for pseudo relative permeability curves of grid blocks have been conducted easily. And these effective parameters are used in equivalent continuum simulations of naturally fractured karst reservoirs. 2. Our two-phase numerical code is based on an efficient full-tensor numerical scheme, in which the pressure equation is discretized by mixed finite element

method and the water saturation equation is discretized by finite volume method. An IMPES sequential solution scheme has been implemented successfully with a restricted CFL condition. 3. We applied fracture and cavity statistics data from the TAHE oilfield outcrop, effective permeability values and other parameters from our numerical code and an equivalent continuum simulator to show that the fluid flow patterns were aligned with the fracture-cavity system. And this new technique permits us to test the sensitivity of the overall flow results to the statistics of the fracture-cavity system. This is important, because the field data are usually statistical and these statistic data about a fracture-cavity system is generally imperfect.

Acknowledgments

This work was supported by the National Basic Research Program of China ("973" Program) (Grant No. 2011CB201004), the Important National Science and Technology Project of China (Grant No. 2011ZX05014-005-003HZ), the National Natural Science Foundation of China (Grant No. 11102237), the Introducing Talents of Discipline to Universities of China (Grant No. B08028), and the Fundamental Research Funds for the Central Universities (Grant No. 27R1102065A). We would also like to thank Dr. Ya-Jun Li for his discussions with us.

References

[1] P. Popov, Y. Efendiev and G. Qin, Multiscale modeling and simulations of flows in naturally fractured karst reservoirs, Commun. Comput. Phys., 6(1) (2009), 162–184.
[2] A. V. Gulbransen, V. L. Hauge and K. A. Lie, A multiscale mixed finite element method for vuggy and naturally fractured reservoirs, SPE J., 15(2) (2010), 395–403.
[3] T. Arbogast and L. H. Lehr, Homogenization of a Darcy-Stokes system modeling vuggy porous media, Comput. Geosci., 10(3) (2006), 291–302.
[4] T. Arbogast and D. S. Brunson, A computational method for approximating a Darcy-Stokes system governing a vuggy porous medium, Comput. Geosci., 11 (2007), 207–218.
[5] P. Popov, G. Qin and L. Bi et al., Multiscale methods for modeling fluid flow through naturally fractured carbonate karst reservoirs, SPE paper 110778, presented at the 2007 SPE Annual Technical Conference and Exhibition, Anaheim, California, USA, 11-14 November, 2007.
[6] P. Popov, L. F. Bi and Y. Efendiev et al., Multiphysics and multiscale methods for modeling fluid flow through naturally fractured carbonate reservoirs, SPE paper 105378, presented at the 15th SPE Middle East Oil & Gas Show and Conference, Bahrain, 11-14 March, 2007.
[7] A. F. Gulbransen, V. L. Hauge and K. A. Lie, A multiscale mixed finite-element method for vuggy and naturally-fractured reservoirs, Paper SPE 119104, presented at the 2009 SPE Reservoir Simulation Symposium, Woodlands, Texas, USA, 2-4 February, 2009.
[8] T. Arbogast and M. S. M. Gomez, A discretization and multigrid solver for a Darcy-Stokes system of three dimensional vuggy porous media, Comput. Geosci., 13 (2009), 331–348.
[9] Z. Q. Huang, J. Yao and Y. J. Li et al., Permeability analysis of fractured vuggy porous media based on homogenization theory, Sci. China Tech. Sci., 53(3) (2010), 839–847.

[10] J. Yao, Z. Q. Huang and Y. J. Li et al., Discrete Fracture-Vug network model for modeling fluid flow in fractured vuggy porous media, Paper SPE 130287-MS, presenred at the International Oil and Gas Conference and Exhibition in China, 8-10 June 2010, Beijing, China, 2010.
[11] Z. Q. Huang, J. Yao and Y. J. Li et al., Numerical calculation of equivalent permeability tensor for fractured vuggy porous media based on homogenization theory, Commun. Comput. Phys., 9(1) (2011), 180–204.
[12] G. Qin, L. F. Bi and P. Popov et al., An efficient upscaling process based on a unified fine-scale multi-physics model for flow simulation in naturally fracture carbonate karst reservoirs, paper SPE132236-MS, presenred at the International Oil and Gas Conference and Exhibition in China, 8-10 June 2010, Beijing, China, 2010.
[13] Y. S. Wu, G. Qin and R. E. Ewing et al., A multiple-continuum approach for modeling multiphase flow in naturally fractured vuggy petroleum reservoirs, Paper SPE 104173, presented at the 2006 SPE International oil & Gas Conference and Exhibition, Beijing, China, 5-7 December, 2006.
[14] Z. J. Kang, Y. S. Wu and J. Li et al., Modeling multiphase flow in naturally fractured vuggy petroleum reservoirs, Paper SPE 102356, presented at the 2006 SPE Annual Technical Conference and Exhibition, San Antonio, Texas, USA, 24-27 September, 2006.
[15] Y. S. Wu, G. Qin and Z. J. Kang et al., A triple-continuum pressure-transient model for a naturally fractured vuggy reservoir, Paper SPE 110044, presented at the 2007 SPE Annual Technical Conference and Exhibition, Anaheim, California, USA, 11-14 November, 2007.
[16] D. Snow, Rock-fracture spacing, openings and porosities, J. Soil Mech. Founda. Div. ASCE., 94 (1968), 73–91.
[17] B. Berkowitz, J. Bear and C. Braester, Continuum models for contaminant transport in fractured porous formations, Water Resour. Res., 24 (1988), 1225–1236.
[18] T. D. Van Golf-Racht, Fundamentals of Fractured Reservoir Engineering, Amsterdam Elsevier, 1982.
[19] T. Nakashima, N. Arihara and S. Sutopo, Effective permeability estimation for modeling naturally fractured reservoirs, Paper SPE 68124, presented at 2001 SPE Middle East Oil Show, Bahrain, 2001.
[20] I. I. Bogdanov, V. V. Mourzenko and J. F. Thovert et al., Effective permeability of fractured porous media in steady state flow, Water Resour. Res., 39(1) (2003), 1023–1040.
[21] I. I. Bogdanov, V. V. Mourzenko and J. F. Thovert et al., Effective permeability of fractured porous media with power-law distribution of fracture sizes, Phys. Rev. E, 76(3) (2007), 036309–036325.
[22] G. S. Beavers and D. D. Joseph, Boundary condition at a naturally permeable wall, J. Fluid Mech., 30 (1967), 197–207.
[23] P. G. Saffman, On the boundary condition at the surface of a porous medium, Stud. Appl. Math., 1 (1971), 93–101.
[24] C. L. Hearn, Simulation of stratified waterflooding by pseudo relative permeability curves, SPE J. Petrol. Tech., 7 (1971), 805–813.
[25] M. S. Talleria, C. J. J. Virues and M. A. Crotti, Pseudo relative permeability functions limitations in the use of the frontal advance theory for 2-dimensional systems, Paper SPE 54004, presented at the SPE Latin American and Caribbean Petroleum Engineering Conference, Caracas, Venezuela, 21-23 April, 1999.
[26] K. Pruess, J. S. Y. Wang and Y. W. Tsang, On the therm.ohydrologic conditions near high-level nuclear wastes emplaced in partially saturated fractured tuff, part 2: effective continuum

approximation, Water Resour. Res., 26(6) (1990), 1249–1261.
[27] P. van Lingen, J. M. Daniel, L. Cosentino and M. Sengul, Single medium simulation of reservoirs with conductive faults and fractures, Paper SPE 68165 presented at the SPE Middle East Oil Show, Bahrain, 17-20 March, 2001.
[28] Rida Abdel-Ghani, Single porosity simulation of fractures with low to medium fracture-to-matrix permeability contrast, Paper SPE 125565, presented at the 2009 SPE/EAGE Reservoir Characterization and Simulation Conference held in Abu Dhabi, UAE, 19-21 October, 2009.
[29] I. Aavatsmark, An introduction to multipoint flux approximations for quadrilateral grids, Comput. Geosci., 6(3-4) (2002), 405–432.
[30] I. Aavatsmark, G. T. Eigestad and R. A. Klausen et al., Convergence of a symmetric MPFA method on quadrilateral grids, Comput. Geosci., 11 (2007), 333–345.
[31] Q. Y. Chen, J. Wan and Y. Yang et al., Enriched multipoint flux approximation for general grids, J. Comput. Phys., 227(3) (2008), 1701–1721.
[32] K. Lipnikov, M. Shashkov and I. Yotov, Local flux mimetic finite difference methods, Numer. Math., 112(1) (2009), 115–152.
[33] P. A. Raviart and J. M. Thomas, A mixed finite element method for second order elliptic equations, Mathematical Aspects of Finite Element Methods (I. Galligani and E. Magenes, eds.), Springer-Verlag, Berlin-Heidelberg-New York, pp. 292–315, 1977.
[34] G. Chavent and J. Jaffre, Mathematical Models and Finite Elements for Reservoir Simulation, North Holland, 1982.
[35] F. Brezzi and M. Fortin, Mixed and Hybrid Finite Element Methods, Springer-Verlag, New York, 1991.
[36] J. E. Aarnes, On the use of a mixed multiscale finite element method for greater flexibility and increased speed or improved accuracy in reservoir simulation, Multiscale Model. Simul., 2(3) (2004), 421–439.
[37] J. E. Aarnes, T. Gimse and K.-A. Lie, An introduction to the numerics of flow in porous media using Matlab, Geometric Modelling, Numerical Simulation and Optimization: Applied Mathematics at SINTEF (G. Hasle, K.-A. Lie and E. Quak, eds.), Springer, Berlin/Heidelberg, pp. 265–306, 2007.
[38] M. Afif and B. Amaziane, On convergence of finite volume schemes for one-dimensional two-phase flow in porous media, J. Comput. Appl. Math., 145 (2002), 31–48.
[39] M. Afif and B. Amaziane, Convergence of finite volume schemes for a degenerate convection-diffusion equation arising in flow in porous media, Comput. Methods Appl. Mech. Eng., 191 (2002), 5265–5286.
[40] M. Afif and B. Amaziane, Numerical simulation of two-phase flow through heterogeneous porous media, Numer. Algorithms, 34 (2003), 117–125.
[41] Z. Q. Huang, J. Yao and Y. Y. Wang et al., Numerical study on two-phase flow through fractured porous media, Sci. China Tech. Sci., 54(9) (2011), 2412–2420.